# Universality in the viscous-to-inertial coalescence of liquid droplets

Xi Xia[a,b], Chengming He[b], and Peng Zhang[b,1]

[a]School of Mechanical Engineering, Shanghai Jiao Tong University, Minhang, Shanghai 200240, P. R. China; and [b]Department of Mechanical Engineering, The Hong Kong Polytechnic University, Hung Hom, Kowloon, Hong Kong 999077

Edited by David A. Weitz, Harvard University, Cambridge, MA, and approved October 14, 2019 (received for review June 30, 2019)

**We present a theory on the coalescence of 2 spherical liquid droplets that are initially stationary. The evolution of the radius of a liquid neck formed upon coalescence was formulated as an initial value problem and then solved to yield an exact solution without free parameters, with its 2 asymptotic approximations reproducing the well-known scaling relations in the inertially limited viscous and inertial regimes. The viscous-to-inertial crossover observed in previous research is also recovered by the theory, rendering the collapse of data of different viscosities onto a single curve.**

droplet coalescence | scaling

Droplet coalescence (1–5) is a ubiquitous phenomenon involved in impact or contact of dispersed 2-phase flows (6–12). Among the various relevant problems, the initial coalescence of 2 liquid droplets has been of core interest. The first quantitative analysis of sphere coalescence was provided by Frenkel (13) based on the assumption of internal Stokes flow; however, the result was commented as "misleading" by Hopper (14), who gave an analytical solution for the coalescence of 2 cylindrical droplets of radius $R_0$ for viscous sintering. His studies (15–17) show that the time evolution of the radius $R$ of the neck (or bridge) between the droplets approximately satisfies $t\sim -R/\ln R^*$ where $R^*=R/R_0$. Later, Eggers et al. (1) considered the 3-dimensional coalescence and attained $R^*\sim -t^*\ln t^*$ for $R^*<0.03$, where $t^*=t/\tau_v$ ($\tau_v=\mu R_0/\sigma$ with $\mu$ and $\sigma$ being the dynamic viscosity of the liquid and the surface tension coefficient, respectively). For larger $R^*$, they (1, 18) argued that the neck flow goes beyond the Stokes regime to the inertial (or inviscid) regime and further arrived at the $1/2$ power-law scaling, $R^*\sim(t/\tau_i)^{1/2}$ with the time scale being $\tau_i=(\rho R_0^3/\sigma)^{1/2}$, where $\rho$ is the liquid density.

Recent advances in the high-speed digital imaging (2, 3, 19), state-of-art probing techniques (4, 20, 21), and numerical simulation (22, 23) enabled researchers to scrutinize the early stages of drop coalescence when $R^*\ll 1$. As a result, the $1/2$ power-law scaling for the inertia-dominated regime was confirmed by many experimental (2, 3, 21, 24–26) and numerical (18, 22, 27–29) studies. The same scaling was also observed for droplet coalescence on substrate (30–32). In the Stokes regime, the exact solution of Hopper (15) has been shown to match well with the experiment of Paulsen et al. (33) and the numerical simulation of Sprittles and Shikhmurzaev (23). However, an intriguing finding by Aarts et al. (2) and Thoroddsen et al. (3) was that the viscous regime of their experiments is well predicted by the linear scaling of $R^*\sim t^*$, which was also corroborated by other studies (4, 19, 25). The apparent inconsistency in the different viscous scalings was clarified by Paulsen et al. (33) who pointed out that the viscous regime should begin with an inertially limited viscous regime, which satisfies the linear scaling, and then be followed by a Stokes regime satisfying Hopper's solution if the viscosity is sufficiently large.

Meanwhile, research attention has been given to the crossover (or transition) from the inertially limited viscous regime to the inertial regime. We hereinafter refer to this crossover as the viscous-to-inertial crossover, which originates from the literature when only 2 coalescence regimes, viscous and inertial, were believed to exist before the identification of the inertially limited viscous regime (33). The first direct evidence of the crossover from $R^*\sim t^*$ to $R^*\sim(t^*)^{1/2}$ was reported by Burton and Taborek (25). By equating the characteristic velocities from the 2 scaling laws, they derived the crossover length, $l_c\sim\mu(R_0/\rho\sigma)^{1/2}$, which was later confirmed by Paulsen and coworkers (4, 34), who further obtained the crossover time, $\tau_c\sim\mu^2(R_0/\rho\sigma^3)^{1/2}$. With these time and length scales, Paulsen et al. (4) applied a fitting curve, $(R/l_c)^{-1}\sim(t/\tau_c)^{-1}+(t/\tau_c)^{-1/2}$, to collapse the neck evolutions of distinct viscosities, which points to a universality in droplet coalescence.

## Theory

We provide a derivation to theoretically explore the universality of the coalescence scaling for the viscous-to-inertial crossover process. A schematic of the neck between 2 merging droplets of initial radius $R_0$ is shown in Fig. 1. The neck radius, $R$, is defined as the minimum radial distance from the $z$ axis to the neck. Under capillary-pressure difference, the neck expands out at a speed of $U(t)$. We assume the flow to be

1) "Quasisteady," meaning the flow acceleration is mainly associated with the convection induced by the neck movement.
2) "Quasiradial," meaning the neck region can be treated as a ring of radius $R$ and width $2r_R$, which is driven by a distributed and quasiradially directed capillary force (1). The capillary force is related to 2 principle curvatures, $1/R$ and $-1/r_R$ (29), with the latter being the effective curvature in the $zr$ plane. As a result, the flow driven by the outwardly moving neck

### Significance

**Most existing literature considers the viscous and inertial regimes of droplet coalescence separately. A recent experiment indicated a universality in the neck-evolution process for coalesced droplets of various viscosities. This work presents a theory that resolves the unified neck evolution in the viscous-to-inertial combined coalescence process. The 2 asymptotic approximations of the theory recover the well-known scaling relations in the inertially limited viscous and the inertial regimes, respectively, with the scaling coefficients predicted explicitly by the solution. Our approach also sets an example of how viscous-to-inertial transition might be dealt with analytically in other similar problems.**

X.X., C.H., and P.Z. performed research; X.X. analyzed data; C.H. performed simulation; X.X. and P.Z. developed theory; and X.X. and P.Z. wrote the paper.

The authors declare no competing interest.

This article is a PNAS Direct Submission.



Data deposition: The data reported in this study have been deposited in the Figshare database, https://doi.org/10.6084/m9.figshare.9947390.v1.

[1]To whom correspondence may be addressed. Email: pengzhang.zhang@polyu.edu.hk.

First published November 5, 2019.

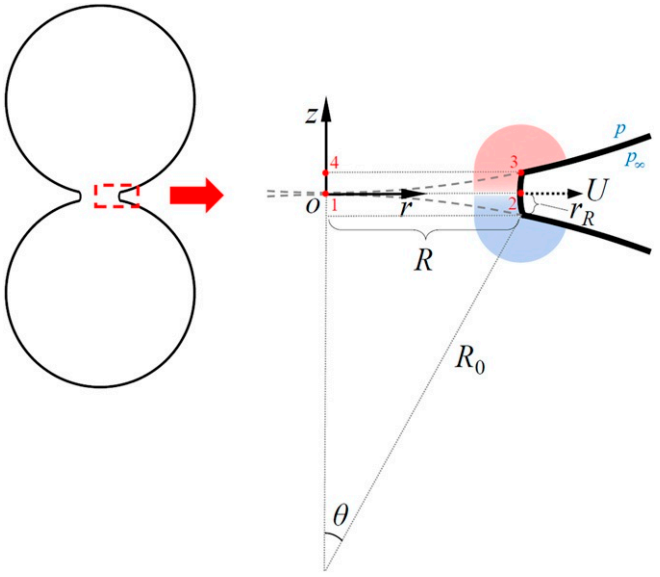


**Fig. 1.** A zoomed-in schematic of the neck region between 2 merging droplets. The red and blue contours illustrate the vorticity distribution localized around the neck.

interface occurs mainly in the radial direction. This is evident from the simulated flow field by Paulsen et al. (33), showing that the streamlines near the neck are predominantly in the radial direction.

3) "Localized," meaning the significant velocity gradients or vorticity distributions are restricted to the vicinity of the neck as illustrated in Fig. 1. This accords with the finding of Paulsen et al. (4) that the flow extends over a length comparable to the neck width rather than the neck radius. Thus, the main vortical structure has a length of $O(r_R)$, and the origin (point 1) is considered as the far field where the velocity gradients are effectively zero. According to Paulsen and coworkers (4, 33), this condition comes naturally for the inertially limited viscous regime, where a Stokes flow is confined around the neck region, while the bulk fluid in the droplet is inertia-dominated; however, this is different from the ideal Stokes regime where the entire droplet is considered to be viscosity-dominated and inertia-negligible.
4) "Geometrically self-similar," so that the neck width satisfies the simple geometric relation, $r_R/R = \tan(\theta/2)$. Under the coalescence regime of $R \ll R_0$, we have $\tan(\theta/2) \approx \theta/2 \approx R/(2R_0)$ and, consequently,

$$\frac{r_R}{R} \approx \frac{R}{2R_0} \ll 1, \qquad [1]$$

which is consistent with previous studies (4, 29). It is noted that this assumption is valid for the inertially limited viscous regime (33), but not for the Stokes regime, where $r_R/R$ has been found to be higher-order small (1, 15).

Assumptions 3 and 4 dictate that the present theory does not apply to the Stokes regime. For the axisymmetric and quasisteady flow, the Navier–Stokes equation in the $r$ direction is expressed as

$$\rho(u_z\partial_z u_r + u_r\partial_r u_r) = -\partial_r p + \mu\left[\partial_z^2 u_r + \partial_r^2 u_r + \partial_r\left(\frac{u_r}{r}\right)\right], \qquad [2]$$

where $u_z$ and $u_r$ are the velocity components in the $z$ and $r$ directions, respectively, and $p$ is the pressure. Along the $r$ axis, $u_z$ and $\partial_z u_r$ are all zeros owing to the condition of symmetry, so the term $u_z\partial_z u_r$ vanishes in Eq. **2**. We now integrate Eq. **2** along the $r$ axis from point 1 $(r=0, z=0)$ to point 2 $(r=R, z=0)$ as

$$\int_{1\to 2}\left[\frac{1}{2}\rho\partial_r u_r^2 + \partial_r p - \mu\left(\partial_z^2 u_r + \partial_r^2 u_r + \partial_r\left(\frac{u_r}{r}\right)\right)\right]\mathrm{d}r$$
$$= \frac{1}{2}\rho U^2 + p_2 - p_1 - \mu\left(\int_0^R \partial_z^2 u_r \mathrm{d}r + (\partial_r u_r)|_2 + \frac{U}{R}\right) = 0, \qquad [3]$$

where the subscripts $_1$ and $_2$ denote the quantities associated with points 1 and 2, respectively. In attaining Eq. **3**, we have also applied $(u_r)|_1 = 0$ according to the axisymmetric condition, $(\partial_r u_r)|_1 = 0$ following assumption 3, and $(u_r)|_2 = U(t)$ by definition. As the present theory concerns the coalescence of liquid droplets in a gaseous environment, the liquid–gas interface can be treated as a free surface, across which the capillary pressure jump is $p_\infty - p = -2\mu\boldsymbol{n}\cdot\boldsymbol{S}\cdot\boldsymbol{n} + \sigma\kappa$ (35), where $p_\infty$ is the ambient gas pressure, $\boldsymbol{n}$ and $\kappa$ are the unit normal vector and curvature of the interface, respectively, and $\boldsymbol{S}$ is the rate-of-strain tensor. Accordingly, the pressures at the far-side droplet and the neck satisfy $p_\infty - p_1 = -2\sigma/R_0$ and $p_\infty - p_2 = -2\mu(\partial_r u_r)|_2 + \sigma(1/r_R - 1/R)$, respectively. Here, $p_1$ serves as the pressure at the far-side droplet according to assumption 3. Subtracting the 2 equations yields $p_2 - p_1 = -\sigma(1/r_R - 1/R + 2/R_0) + 2\mu(\partial_r u_r)|_2$, which can be plugged into Eq. **3** to obtain

$$\frac{1}{2}\rho U^2 - \sigma\left(\frac{1}{r_R} - \frac{1}{R} + \frac{2}{R_0}\right)$$
$$-\mu\left(\int_0^R \partial_z^2 u_r \mathrm{d}r + (\partial_z u_z)|_2 + \frac{2U}{R}\right) = 0. \qquad [4]$$

Note that the continuity equation, $\partial_z u_z + \partial_r u_r + u_r/r = 0$, has been used in the above derivation.

The quasiradial assumption 2 implies $u_z = 0$ around point 2 and further $(\partial_z u_z)|_2 = 0$ in Eq. **4**. Furthermore, $\partial_z^2 u_r$ can be expressed as

$$\partial_z^2 u_r \approx \frac{(\partial_z u_r)|_{z=r_R} - (\partial_z u_r)|_{z=0}}{r_R} = \frac{(\partial_r u_z + \omega)|_{z=r_R}}{r_R}, \qquad [5]$$

with $(\partial_z u_r)|_{z=0} = 0$ by axisymmetry and $\omega = \partial_z u_r - \partial_r u_z$ being the vorticity. Eq. **5** essentially gives a leading-order approximation based on linearizing the strain rate near the plane of

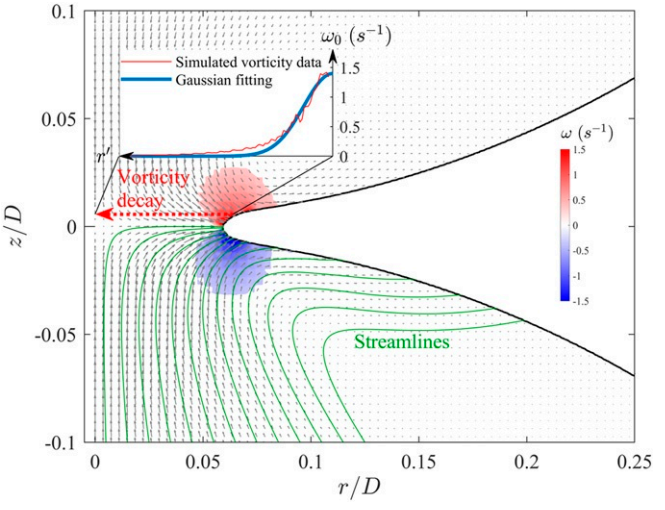


**Fig. 2.** The simulated flow field around the neck for a representative case of $Oh = 4$. The numerical method is reported in *Materials and Methods*.

symmetry. Integrating Eq. **5** from point 4 ($r=0, z=r_R$) to point 3 ($r=R, z=r_R$) yields

$$\int_0^R \partial_z^2 u_r \mathrm{d}r \approx \frac{1}{r_R}\left((u_z)|_4^3 + \int_0^R \omega|_{z=r_R}\mathrm{d}r\right), \qquad [6]$$

where $(u_z)|_3$ and $(u_z)|_4$ are negligibly small according to assumptions 2 and 3, respectively. For $(u_z)|_3$, the continuity equation gives $(\partial u_z/\partial z)|_3 \sim U/R$, which amounts to $(u_z)|_3/r_R \sim U/R$. For $(u_z)|_4$, it must be smaller than $\bar{u}_z$, which is the average $u_z$ across the 3–4 interface and is estimated to be $O(Ur_R/R)$ by applying the integral form of the continuity equation to the revolved rectangular 1234. Therefore, both $(u_z)|_3$ and $(u_z)|_4$ are bounded by $O(Ur_R/R)$.

Lacking a priori knowledge of the vorticity field, we seek an approximation of $\omega|_{z=r_R}$ based on the computational observation that in the $orz$ plane, the neck movement induces 2 opposite-sign vortices that are centered around the 2 edges of the neck, as illustrated in Fig. 2. This physical picture is also consistent with assumption 3. The radial-vorticity decay displayed in Fig. 2 further implies that the vortex is analogous to a Batchelor vortex (36) and has a Gaussian vorticity distribution as

$$\omega_0(r') = \frac{U}{r_v} e^{-\left(\frac{r'}{r_v}\right)^2}, \qquad [7]$$

where $r' = R - r$ is the radial location relative to the vortex center located at the neck interface, and $r_v$ is an effective radius of the vortex core. Eq. **7** is also similar to the Oseen–Lamb vortex (37), which is an analytical solution to the vorticity-diffusion equation. Recognizing that $\omega_0(r') = \omega(r) = \omega(R-r')$ for $z=r_R$ and $0 \le r \le R$, the integral on the right-hand side of Eq. **6** can be further derived as

$$-U\int_0^{\frac{R}{r_v}} e^{-\left(\frac{r'}{r_v}\right)^2}\mathrm{d}\left(\frac{r'}{r_v}\right) = -\frac{\sqrt{\pi}U}{2}\mathrm{erf}\left(\frac{R}{r_v}\right) \approx -\frac{\sqrt{\pi}U}{2}, \qquad [8]$$

with $R/r_v \gg 1$ given by assumption 3 and Eq. **1**.

We now plug in Eqs. **6** and **8** to cast Eq. **4** in the form,

$$\frac{1}{2}\rho U^2 - \sigma\left(\frac{1}{r_R} - \frac{1}{R} + \frac{2}{R_0}\right) - \mu\left(-\frac{\sqrt{\pi}U}{2r_R} + O\left(\frac{U}{R}\right)\right) = 0. \qquad [9]$$

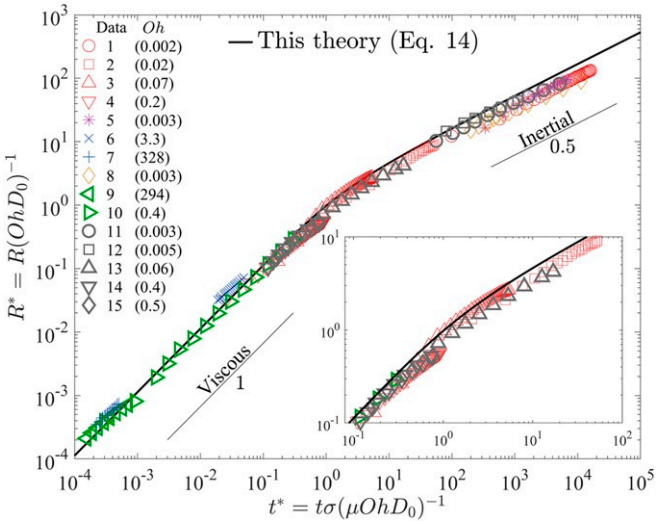


**Fig. 3.** Model validation against experimental data from previous studies (see *Experimental Data* in *Materials and Methods* for detailed parameters). A close-up of the crossover regime is shown in the *Inset* plot.

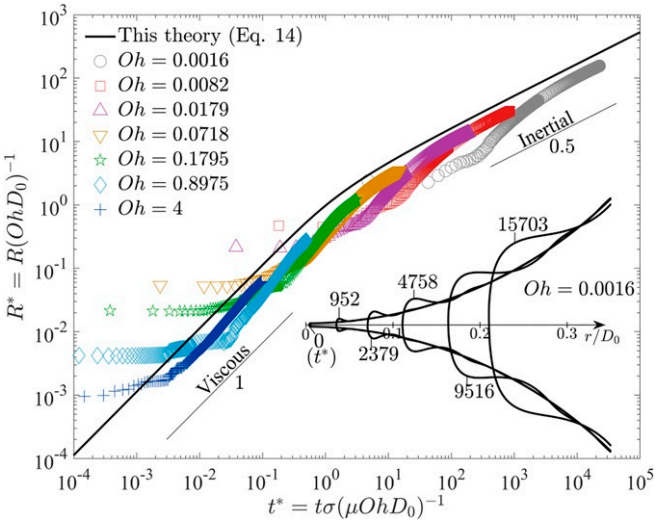


**Fig. 4.** Validation of the current theory (Eq. **14**) against simulated neck evolution for droplets of different viscosities (*Oh*). Inset plot shows the time evolution of the simulated neck interface for a representative case with $Oh = 0.0016$.

Applying Eq. **1** and balancing the leading-order terms of Eq. **9** yields

$$\rho U^2 - \frac{4\sigma R_0}{R^2} + \frac{2\sqrt{\pi}\mu R_0 U}{R^2} = 0, \qquad [10]$$

which can be combined with $\dot{R} = \mathrm{d}R/\mathrm{d}t = U$ to derive

$$\frac{\rho \dot{R}^{*2} L^2}{T^2} - \frac{2\sigma D_0}{R^{*2}L^2} + \frac{\sqrt{\pi}\mu D_0 \dot{R}^*}{R^{*2}LT} = 0, \qquad [11]$$

where $D_0 = 2R_0$, $R^* = R/L$, $\dot{R}^* = \dot{R}/U$, and $T = L/U$, with $L$, $U$, and $T$ being the characteristic length, velocity, and time scales, respectively.

Paulsen and coworkers (4, 34) showed that by using proper time and length scales for nondimensionalization, their droplet coalescence data of various viscosities can be collapsed onto a single curve, implying the existence of a unified formula for the viscous-to-inertial combined regimes. Let Eq. **11** be such a formula, it must be free of dimensional parameters, so we have

$$\frac{\rho L^2}{T^2} = \frac{\sigma D_0}{L^2} = \frac{\mu D_0}{LT}, \qquad [12]$$

yielding $L = OhD_0$ and $T = \mu OhD_0/\sigma$, where $Oh = \mu/\sqrt{\rho\sigma D_0}$ is the Ohnesorge number. Note that $L$ and $T$ match exactly with the viscous-to-inertial crossover scales found by previous studies (4, 25, 34). Accordingly, Eq. **11** takes the dimensionless form,

$$\dot{R}^{*2} - \frac{2}{R^{*2}} + \frac{\sqrt{\pi}\dot{R}^*}{R^{*2}} = 0. \qquad [13]$$

We can integrate Eq. **13** with the initial condition $R^*(t^*=0) = 0$, where $t^* = t/T$, to obtain the exact solution,

$$t^* = \frac{\sqrt{\pi}R^*}{4} + \frac{\sqrt{\pi}}{8}\left[R^*\sqrt{\frac{8R^{*2}}{\pi}+1} + \frac{\sqrt{\pi}}{2\sqrt{2}}\sinh^{-1}\left(\frac{2\sqrt{2}R^*}{\sqrt{\pi}}\right)\right]. \qquad [14]$$

Eq. **14** readily gives the asymptotic behaviors associated with the inertially limited viscous and inertial regimes. For the inertial regime, $R^* \gg \sqrt{2\pi}/4$, Eq. **14** yields

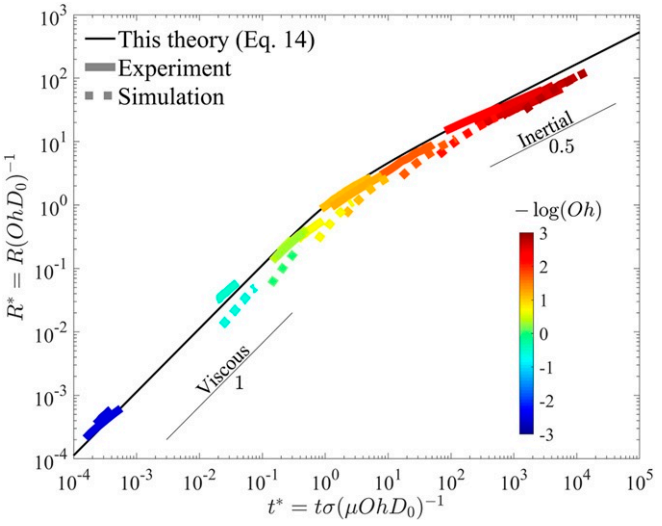


**Fig. 5.** Demonstration of the dominant role of *Oh* in deciding the coalescence regimes. All datasets in Figs. 3 and 4 are dyed with a color map based on log(*Oh*). To indicate the late-stage development, only data in the range of $0.1 \leq R/D_0 \leq 0.2$ are plotted for each coalescence case.

$$t^* \approx \frac{R^{*2}}{2\sqrt{2}} + O(R^*). \quad [15]$$

For the inertially limited viscous regime, $R^* \ll \sqrt{2\pi}/4$, Eq. **14** yields

$$t^* \approx \frac{\sqrt{\pi}}{4}\left[\frac{3R^*}{2} + \frac{\sqrt{\pi}}{4\sqrt{2}}\ln\left(\frac{2\sqrt{2}R^*}{\sqrt{\pi}} + 1\right)\right] \approx \frac{\sqrt{\pi}R^*}{2} + O(R^{*2}). \quad [16]$$

Eq. **16** can be also reduced to the form of $R \sim t\sigma/\mu$, which is void of any characteristic length. This can be interpreted that the physics of the viscous regime is self-similar in an intermediate-asymptotic sense (38).

## Results and Discussion

To evaluate our theory, we first write Eq. **15** in the dimensional form of $R/R_0 \approx c_1(t/\tau_i)^{1/2}$ with $c_1 = 2$, which recovers the $1/2$ power-law scaling for the inertial regime. Similarly, Eq. **16** can be expressed in the dimensional form of $R/R_0 \approx c_2 t/\tau_v$ with $c_2 = 2/\sqrt{\pi}$, which gives the linear scaling relation in the inertially limited viscous regime. These theoretical coefficients agree reasonably well with $c_1 = 1.68$ and $c_2 = 1$, which were obtained by empirical fitting (34).

We next validate our theory against experimental data from literature. Fig. 3 shows existing experimental data of various $Oh$, corresponding to a variety of fluid types, such as water, silicon oil, and glycerol–salt–water mixture, that are of distinct fluid properties as provided in *Materials and Methods*. It is observed that all data tend to collapse onto a single curve, well predicted by the current theory. Considering the assumptions and approximations made in the derivation, the agreement between theory and experiment is quite satisfactory. The theory also captures the asymptotic behaviors of the data in the inertially limited viscous and inertial regimes. Specifically, the $R^* \sim t^*$ and $R^* \sim \sqrt{t^*}$ scaling relations show up as $R^* \ll 1$ and $R^* \gg 1$, respectively, whereas a clear inflection point can be identified around $R^* \sim O(1)$ and $t^* \sim O(1)$ , marking the transition from viscous to inertial. It should be emphasized that, although empirical (34) and semiempirical (39) models exist previously, this work presents a theory that resolves the unified scaling in the viscous-to-inertial combined coalescence process.

We now provide further validation of the theory against droplet-coalescence simulations of various viscosities. The simulation setup is specified in *Materials and Methods*. The neck-interface evolution for a representative case of $Oh = 0.0016$ is shown in the inset plot of Fig. 4. Similar simulations were conducted for $Oh = 0.0082$, 0.0179, 0.0718, 0.1795, 0.8975, and 4. The corresponding neck-radius evolutions are presented in the main plot of Fig. 4. It is seen that each simulation dataset originates from a finite neck radius, causing the simulated evolution to deviate from the theory at the beginning. Nevertheless, the later-stage coalescence behavior is less affected by the simulation onset, as each neck-evolution curve gradually approaches and then follows its designated scaling, showing that the overall trend of the simulation curves are well captured by the theory. Similar neck evolution behaviors were also observed from previous simulations (22, 40). The source of the discrepancy between simulation and theory could be 2-fold. The first is directly associated with the onset of the numerical neck radius being nonzero, which can be translated into a time offset as if the neck radius were to grow from zero. The second is related to the initial velocity of the neck, which is

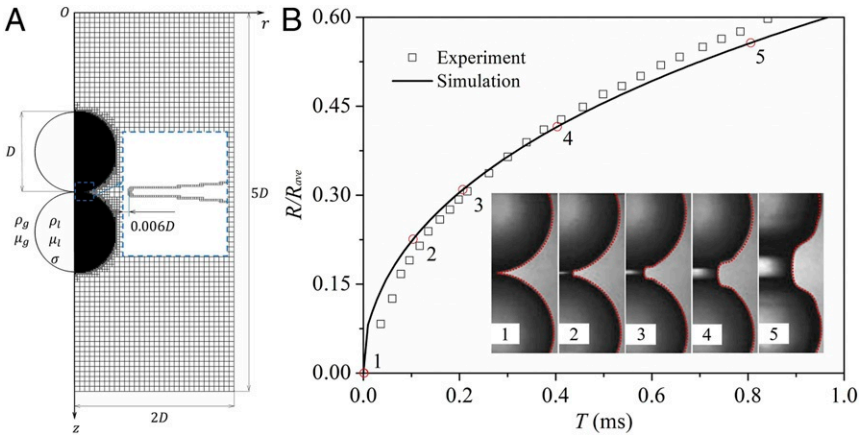


**Fig. 6.** (*A*) Computational domain and mesh for the droplet coalescence simulation, with the inset plot showing the zoomed-in grid configuration of the interface near the initial contact point. (*B*) Simulated droplet coalescence vs. Thoroddsen et al.'s experiment (3) ($Oh = 2.5 \times 10^{-3}$). The main plot compares the coalescence speed and the subplot images compares the deformation of the droplet interface, with the red-dotted contours representing the simulation results. Note that the average radius, $R_{ave}$, of the 2 droplets was used in the original experiment to account for a slight size disparity between the 2 droplets.

**Table 1. Parameters ($D_0$, $\rho$, $\sigma$, and $\mu$) for the 15 sets of experimental data plotted in Fig. 3**

| Data source | Fluid type | $D_0$ ($\times 10^{-3}$), m | $\rho$, kg m$^{-3}$ | $\sigma$ ($\times 10^{-2}$), N m$^{-1}$ | $\mu$ ($\times 10^{-3}$), Pa·s |
|---|---|---|---|---|---|
| 1-Aarts et al. (2) | Water | 4.0 | 997 | 7.2 | 1 |
| 2-Aarts et al. (2) | Silicon oil | 4.0 | 970 | 2.0 | 5 |
| 3-Aarts et al. (2) | Silicon oil | 4.0 | 970 | 2.0 | 20 |
| 4-Aarts et al. (2) | Silicon Oil | 4.0 | 970 | 2.0 | 50 |
| 5-Thoroddsen et al. (3) | Water | 2.2 | 997 | 7.2 | 1 |
| 6-Yao et al. (19) | Silicon oil | 10.0 | 970 | 0.9 | 970 |
| 7-Yao et al. (19) | Silicon oil | 10.0 | 970 | 0.9 | 97,000 |
| 8-Fezzaa and Wang (21) | Water | 1.99 | 997 | 7.2 | 1 |
| 9-Paulsen et al. (33) | Silicon oil | 2.0 | 970 | 2.0 | 58,000 |
| 10-Paulsen et al. (33) | GSW | 4.0 | 1,200 | 6.5 | 230 |
| 11-Paulsen (34) | GSW | 4.0 | 1,182 | 8.9 | 1.9 |
| 12-Paulsen (34) | Silicon oil | 2.2 | 818 | 1.7 | 0.82 |
| 13-Paulsen (34) | GSW | 4.0 | 1,225 | 5.5 | 30 |
| 14-Paulsen (34) | GSW | 4.0 | 1,230 | 6.3 | 230 |
| 15-Paulsen (34) | Silicon oil | 2.2 | 966 | 2.1 | 97 |

GSW, glycerol–salt–water mixture.

set as zero in the simulation as indicated from Fig. 4; however, the theory predicts that the neck velocity is nonzero at the same radius. Therefore, this velocity difference in turn causes additional difference in the neck evolution. It should be noted that the precise setup of initial condition in both simulation and theory requires information about droplet "touching" at earlier times and smaller scales. Whether such "very-early" droplet coalescence can be resolved in the framework of continuum mechanics is questionable and beyond the scope of the present work.

Furthermore, this theory suggests that $R^* = R/(OhD_0)$ is a criterion segmenting the different coalescence regimes. Although it involves both $R/D_0$ and $Oh$, for different fluids, $Oh$ is the parameter that eventually decides whether the inertial regime could arrive. This is evident from Fig. 5, showing that data in the inertial regime generally corresponds to $Oh \ll 1$ and vice versa. This criterion has important practical use. For example, Aarts et al. (2) considered Data 3 (20 mPa s silicon oil) and Data 4 (50 mPa s silicon oil) to be within the inertial regime, whereas Fig. 3 clearly shows that Data 3 mainly covers the crossover regime and Data 4 extends from the inertially limited viscous regime to the crossover regime.

In summary, this study presents a unified theory to support the prominent scaling laws as well as the crossover behaviors observed from previous experimental studies of binary droplet coalescence. There are a few key innovations that are crucial to the development of this theory. The first one is integrating the governing Navier–Stokes equation along the radial direction to connect the local movement of the neck to the dynamics of the bulk droplet. This enables us to resolve the inertially limited viscous regime, which is locally viscous but inertially driven in a global sense. The same approach could be useful in solving other similar crossover problems that involve different physics at different scales. The second innovation is converting the velocity gradients to vorticity, which provides a more physical picture of the "localized flow" around the neck region. Based on the updated vortex-dynamical perspective, the third innovation is to apply the Batchelor vortex model to account for the neck vortices. These innovations together result in the quantitative estimation of the scaling parameters, which is a unique contribution of this work and is beyond the capacity of a simple scaling analysis. However, as the present theory does not concern the Stokes regime, future work is required to address the transition between the inertially limited viscous regime and the Stokes regime.

## Materials and Methods

**Numerical Approach.** Numerical simulation was adopted to help understand the detailed physics of droplet coalescence and could produce data of arbitrary properties that would not be easily obtained by experiment. To this end, the volume of fluid (VOF) simulation (41, 42) was implemented using the open source code Gerris (43, 44). This numerical approach has been demonstrated to be suitable for multiphase flow involving the dynamics of droplets (12, 45–51).

The simulation setup for the coalescence of 2 equal-sized droplets is illustrated in Fig. 6*A*. It is noted that the present study concerns the situation where the density and viscosity of the gas phase are orders of magnitude smaller than those of the liquid phase and that the droplets are assumed to be initially stationary and touching with each other, so no gas film effect (7, 52, 53) is involved. Thus, the density and viscosity ratios have negligible effect on the coalescence result, and the only controlling parameter is the nondimensional liquid viscosity, known as the Ohnesorge number, defined as $Oh = \mu/\sqrt{\rho\sigma D_0}$. A major challenge here is reducing the initial neck radius $R$ upon the touching of 2 droplets at $t = 0$. $R(t = 0)$ is nonzero in this simulation because the numerical interface is represented by finite layers of grid cells in the VOF framework. To this end, we have employed the adaptive mesh refinement (43, 44) to bring down the initial neck radius, $R/D_0$, to the order of $O(10^{-3})$. Fig. 6*B* presents a validation case, which compares our simulation with Thoroddsen et al.'s experiment (3) of water droplet coalescence in air. The main plot compares the coalescence speed of the neck radius, showing a generally good agreement between the numerical prediction and the experimental data. Furthermore, the subplot images also demonstrate that in an evolution sequence our simulated droplet interfaces, which are marked with the red-dotted contours, all match well with the experimental droplet profiles.

**Experimental Data.** This work collects the experimental data of previous droplet coalescence studies for model validation. Specifically, Data 1 to Data 4 were from Aarts et al. (2), Data 5 from Thoroddsen et al. (3), Data 6 and Data 7 from Yao et al. (19), Data 8 from Fezzaa and Wang (21), Data 9 and Data 10 from Paulsen et al. (33), and Data 11 to Data 15 from Paulsen (34). These correspond to a variety of fluid types, such as water, silicon oil, and glycerol–water–NaCl mixture, that are of distinct fluid properties. The diameter of the droplet $D_0$, the density $\rho$, the surface tension coefficient $\sigma$, and the dynamic viscosity $\mu$ for the 15 sets of data are reported in Table 1.

**Data Sharing.** The data reported in this study were obtained through numerical simulation, as specified in *Numerical Approach*. The entire dataset for generating Figs. 2, 4, and 6 have been deposited in the Figshare database (54) and shared with the public.

**ACKNOWLEDGMENTS.** We acknowledge support from the Hong Kong Research Grants Council/General Research Fund (Grants PolyU 152217/14E and PolyU 152651/16E) and the "Open Fund" of State Key Laboratory of Engines (Tianjin University, Grant K2018-12).

1. J. Eggers, J. R. Lister, H. A. Stone, Coalescence of liquid drops. *J. Fluid Mech.* **401**, 293–310 (1999).
2. D. G. A. L. Aarts, H. N. W. Lekkerkerker, H. Guo, G. H. Wegdam, D. Bonn, Hydrodynamics of droplet coalescence. *Phys. Rev. Lett.* **95**, 164503 (2005).
3. S. T. Thoroddsen, K. Takehara, T. G. Etoh, The coalescence speed of a pendent and a sessile drop. *J. Fluid Mech.* **527**, 85–114 (2005).
4. J. D. Paulsen, J. C. Burton, S. R. Nagel, Viscous to inertial crossover in liquid drop coalescence. *Phys. Rev. Lett.* **106**, 114501 (2011).
5. X. Xia, C. He, D. Yu, J. Zhao, P. Zhang, Vortex-ring-induced internal mixing upon the coalescence of initially stationary droplets. *Phys. Rev. Fluids* **2**, 113607 (2017).
6. A. L. Yarin, Drop impact dynamics: Splashing, spreading, receding, bouncing. . .. *Annu. Rev. Fluid Mech.* **38**, 159–192 (2006).
7. P. Zhang, C. K. Law, An analysis of head-on droplet collision with large deformation in gaseous medium. *Phys. Fluids* **23**, 042102 (2011).
8. M. J. Thoraval *et al.*, von Varman vortex street within an impacting drop. *Phys. Rev. Lett.* **108**, 264506 (2012).
9. T. Tran, H. de Maleprade, C. Sun, D. Lohse, Air entrainment during impact of droplets on liquid surfaces. *J. Fluid Mech.* **726**, R3 (2013).
10. H. P. Kavehpour, Coalescence of drops. *Annu. Rev. Fluid Mech.* **47**, 245–268 (2015).
11. C. Tang, J. Zhao, P. Zhang, C. K. Law, Z. Huang, Dynamics of internal jets in the merging of two droplets of unequal sizes. *J. Fluid Mech.* **795**, 671–689 (2016).
12. C. He, X. Xia, P. Zhang, Non-monotonic viscous dissipation of bouncing droplets undergoing off-center collision. *Phys. Fluids* **31**, 052004 (2019).
13. J. J. Frenkel, Viscous flow of crystalline bodies under the action of surface tension. *J. Phys.* **9**, 385–431 (1945).
14. R. W. Hopper, Coalescence of two viscous cylinders by capillarity: Part I, theory. *J. Am. Ceram. Soc.* **76**, 2947–2952 (1993).
15. R. W. Hopper, Coalescence of two equal cylinders: Exact results for creeping viscous plane flow driven by capillarity. *J. Am. Ceram. Soc.* **67**, 262–264 (1984).
16. R. W. Hopper, Plane Stokes flow driven by capillarity on a free surface. *J. Fluid Mech.* **213**, 349–375 (1990).
17. R. W. Hopper, Stokes flow of a cylinder and half-space driven by capillarity. *J. Fluid Mech.* **243**, 171–181 (1992).
18. L. Duchemin, J. Eggers, C. Josseran, Coalescence of liquid drops. *J. Fluid Mech.* **487**, 167–178 (2003).
19. W. Yao, H. J. Maris, P. Pennington, G. M. Seidel, Coalescence of viscous liquid drops. *Phys. Rev. E* **71**, 016309 (2005).
20. S. C. Case, S. R. Nagel, Coalescence in low-viscosity liquids. *Phys. Rev. Lett.* **100**, 084503 (2008).
21. K. Fezzaa, Y. Wang, Ultrafast x-ray phase-contrast imaging of the initial coalescence phase of two water droplets. *Phys. Rev. Lett.* **100**, 104501 (2008).
22. J. E. Sprittles, Y. D. Shikhmurzaev, Coalescence of liquid drops: Different models versus experiment. *Phys. Fluids* **24**, 122105 (2012).
23. J. E. Sprittles, Y. D. Shikhmurzaev, A parametric study of the coalescence of liquid drops in a viscous gas. *J. Fluid Mech.* **753**, 279–306 (2014).
24. M. Wu, T. Cubaud, C. M. Ho, Scaling law in liquid drop coalescence driven by surface tension. *Phys. Fluids* **16**, L51–L54 (2004).
25. J. C. Burton, P. Taborek, Role of dimensionality and axisymmetry in fluid pinch-off and coalescence. *Phys. Rev. Lett.* **98**, 224502 (2007).
26. S. C. Case, Coalescence of low-viscosity fluids in air. *Phys. Rev. E* **79**, 026307 (2009).
27. R. T. Eiswirth, H. J. Bart, A. A. Ganguli, E. Y. Kenig, Experimental and numerical investigation of binary coalescence: Liquid bridge building and internal flow fields. *Phys. Fluids* **24**, 062108 (2012).
28. J. C. Pothier, L. J. Lewis, Molecular-dynamics study of the viscous to inertial crossover in nanodroplet coalescence. *Phys. Rev. B* **85**, 115447 (2012).
29. M. Gross, I. Steinbach, D. Raabe, F. Varnik, Viscous coalescence of droplets: A lattice Boltzmann study. *Phys. Fluids* **25**, 052101 (2013).
30. W. D. Ristenpart, P. M. McCalla, R. V. Roy, H. A. Stone, Coalescence of spreading droplets on a wettable substrate. *Phys. Rev. Lett.* **97**, 064501 (2006).
31. J. F. Hernández-Sánchez, L. A. Lubbers, A. Eddi, J. H. Snoeijer, Symmetric and asymmetric coalescence of drops on a substrate. *Phys. Rev. Lett.* **108**, 184502 (2012).
32. A. Eddi, K. G. Winkels, J. H. Snoeijer, Influence of droplet geometry on the coalescence of low viscosity drops. *Phys. Rev. Lett.* **111**, 144502 (2013).
33. J. D. Paulsen *et al.*, The inexorable resistance of inertia determines the initial regime of drop coalescence. *Proc. Natl. Acad. Sci. U.S.A.* **109**, 6857–6861 (2012).
34. J. D. Paulsen, Approach and coalescence of liquid drops in air. *Phys. Rev. E* **88**, 063010 (2013).
35. G. Tryggvason, R. Scardovelli, S. Zaleski, "Fluid mechanics with interfaces" in *Direct Numerical Simulations of Gas-Liquid Multiphase Flows* (Cambridge University Press, Cambridge, UK, 2011), pp. 39–40.
36. G. K. Batchelor, Axial flow in trailing line vortices. *J. Fluid Mech.* **20**, 645–658 (1964).
37. J. Z. Wu, H. Y. Ma, M. D. Zhou, "Typical vortex solutions" in *Vorticity and Vortex Dynamics* (Springer, 2006), pp. 262–263.
38. G. I. Barenblatt, "The construction of intermediate-asymptotic solutions using dimensional analysis. Self-similar solutions" in *Scaling, Self-Similarity, and Intermediate Asymptotics* (Cambridge University Press, Cambridge, UK, 1996), pp. 86–94.
39. X. Xia, C. He, P. Zhang, Scalings in coalescence of liquid droplets. arXiv:1803.05789 (31 December 2018).
40. J. E. Sprittles, Y. D. Shikhmurzaev, The coalescence of liquid drops in a viscous fluid: Interface formation model. *J. Fluid Mech.* **751**, 480–499 (2014).
41. R. Scardovelli, S. Zaleski, Direct numerical simulation of free-surface and interfacial flow. *Annu. Rev. Fluid Mech.* **31**, 567–603 (1999).
42. G. Tryggvason, A. Esmaeeli, J. Lu, S. Biswas, Direct numerical simulations of gas/liquid multiphase flows. *Fluid Dyn. Res.* **38**, 660–681 (2006).
43. S. Popinet, Gerris: A tree-based adaptive solver for the incompressible Euler equations in complex geometries. *J. Comput. Phys.* **190**, 572–600 (2003).
44. S. Popinet, An accurate adaptive solver for surface-tension-driven interfacial flows. *J. Comput. Phys.* **228**, 5838–5866 (2009).
45. X. Chen, V. Yang, Thickness-based adaptive mesh refinement methods for multi-phase flow simulations with thin regions. *J. Comput. Phys.* **269**, 22–39 (2014).
46. X. Chen, V. Yang, Effect of ambient pressure on liquid swirl injector flow dynamics. *Phys. Fluids* **26**, 102104 (2014).
47. G. Agbaglah *et al.*, Drop impact into a deep pool: Vortex shedding and jet formation. *J. Fluid Mech.* **764**, R1 (2015).
48. M. J. Thoraval, Y. Li, S. T. Thoroddsen, Vortex-ring-induced large bubble entrainment during drop impact. *Phys. Rev. E* **93**, 033128 (2016).
49. S. Wildeman, C. W. Visser, C. Sun, D. Lohse, On the spreading of impacting drops. *J. Fluid Mech.* **805**, 636–655 (2016).
50. Z. Jian, C. Josserand, S. Popinet, P. Ray, S. Zaleski, Two mechanisms of droplet splashing on a solid substrate. *J. Fluid Mech.* **835**, 1065–1086 (2018).
51. R. Cimpeanu, M. R. Moore, Early-time jet formation in liquid–liquid impact problems: Theory and simulations. *J. Fluid Mech.* **856**, 764–796 (2018).
52. J. de Ruiter, J. M. Oh, D. van den Ende, F. Mugele, Dynamics of collapse of air films in drop impact. *Phys. Rev. Lett.* **108**, 074505 (2012).
53. J. Li, Macroscopic model for head-on binary droplet collisions in a gaseous medium. *Phys. Rev. Lett.* **117**, 214502 (2016).
54. X. Xia, C. He, P. Zhang, Simulation data for the neck evolution in liquid droplet coalescence. Figshare. https://doi.org/10.6084/m9.figshare.9947390.v1. Deposited 8 October 2019.